Chemical Engineering Journal 446 (2022) 136723

Contents lists available at ScienceDirect

Chemical Engineering Journal

journal homepage: www.elsevier.com/locate/cej

An experimental, theoretical and kinetic-modeling study of hydrogen sulfide pyrolysis and oxidation

Alessandro Stagni [a,1,*], Suphaporn Arunthanayothin [b,1], Luna Pratali Maffei [a], Olivier Herbinet [b], Frédérique Battin-Leclerc [b], Tiziano Faravelli [a]

[a] Department of Chemistry, Materials, and Chemical Engineering "G. Natta", Politecnico di Milano, Milano 20133, Italy
[b] Laboratoire Réactions et Génie des Procédés, CNRS-Université de Lorraine, 1 rue Grandville, 54000 Nancy, France

ARTICLE INFO

Keywords:
Hydrogen sulfide
Sulphur oxides
Jet-stirred reactor
Flow reactor
Ab initio
Detailed kinetics

ABSTRACT

Hydrogen sulfide chemistry has recently undergone a renewed interest due to the current energy transition, requiring a proper treatment of such impurities in the sources like shale gas or biogas. Moreover, the lower-temperature, diluted conditions considered nowadays for reducing pollutant emissions require a wider-range development and validation of the pyrolysis and oxidation mechanisms. In this work, this was addressed through an experimental campaign carried out in three reactor facilities, namely a jet-stirred reactor and two flow reactors. A wide range of operating conditions could thus be covered, in terms of equivalence ratios under lean conditions ($0.018 \leq \Phi \leq 0.5$), temperatures ($400\,K \leq T \leq 2000\,K$) and residence times ($0.1\,s \leq \tau \leq 2\,s$). The mole fractions of reactants (H_2S, O_2), products (SO_2, H_2O) and intermediates (H_2) were measured. In parallel, a kinetic mechanism of H_2S pyrolysis and oxidation was developed by including the latest available kinetic rates on sulfur pyrolysis and oxidation chemistry, which were added to a core H_2/O_2 module, previously validated. Such a mechanism included a re-evaluation of selected key reaction steps, identified via sensitivity analysis. Results showed a general agreement of the experimental measurements with predictions: in the case of pyrolysis, the thermal decomposition reaction ($H_2S + M = H_2 + S + M$) was identified as the sole controlling step: a critical choice of the kinetic rate had to be made, due to the significant disagreement among the literature rates. Concerning oxidation, the H-abstraction from H_2S by O_2 was found to be the major bottleneck at the lowest temperatures, with HO_2 becoming a key abstractor, too, under very lean conditions. At higher temperatures, a key role was played instead by the H-abstraction of H_2S with S ($H_2S + S = SH + SH$), acting in the reverse direction and providing S radicals, boosting the oxidation process.

1. Introduction

The recent diversification of the world energy portfolio through the inclusion of unconventional fuels has raised the issue of controlling the pollutant emissions, resulting from their combustion. They include, for example, Nitrogen Oxides (NO_x) [1], Volatile Organic Compounds (VOCs) [2], and finally Sulfur Oxides (SO_x), mostly originated by Hydrogen Sulfide (H_2S) [3]. H_2S has been matter of noteworthy interest in the last decades and is regulated at a legislative level [4], primarily because of its harmful effects on the human health [5], corrosive power and catalyst deactivation [6]. As a matter of fact, significant research is being devoted on its neutralization, due to the variety of the sources: it is contained in non-negligible amounts in some natural gas reservoirs, and the transition to shale gas and bio-gas has amplified the issue, since in these cases its concentration may even arrive to thousands of parts per million (ppm) [7]. In addition, H_2S also constitutes a by-product of the oil refinery industry, where it is usually treated via the Claus process [8]. As a result, the significant presence of H_2S in these raw materials has brought about a renewed interest in its combustion chemistry, which has been matter of extensive studies in the latest two decades. Moreover, past works have shown that chemical interactions between H_2S and hydrogen [9], as well as H_2S and hydrocarbons [10,11], modify the reactivity of the fuel mixture.

Due to safety issues, the experimental characterization of H_2S combustion has often been difficult to perform, and until recently literature has not been particularly rich in dedicated datasets. The earliest experiments concerned its laminar flame speed at atmospheric pressure

* Corresponding author.
E-mail address: alessandro.stagni@polimi.it (A. Stagni).
[1] These authors contributed equally to this work.

https://doi.org/10.1016/j.cej.2022.136723

Available online 2 May 2022

Nomenclature

Roman symbols

P	Pressure [Pa]
T	Temperature [K]
X	Mole fraction [-]

Greek symbols

τ	Residence time [s]
Φ	Equivalence ratio [-]

Acronyms

AS	Active Space
C/VTST	Conventional/Variational Transition State Theory
CBS	Complete Basis Set
DF	Density Fitted
DFT	Density Functional Theory
IRC	Intrinsic Reaction Coordinate
ISC	InterSystem Crossing
JSR	Jet Stirred Reactor
ME	Master Equation
MEP	Minimum Energy Path
MR	Multi-reference
MRCI	Multi-reference configuration interaction
NO_x	Nitrogen Oxides
PES	Potential Energy Surface
ppm	parts per million
RRHO	Rigid Rotor Harmonic Oscillator
SO_x	Sulfur Oxides
TS	Transition State
VOC	Volatile Organic Compounds
VRC-TST	Variable Reaction Coordinate – Transition State Theory
ZPE	Zero Point Energy
1DHR	One-dimensional hindered rotor

[12–15] and speciation in laminar premixed flames [16,17]. More recently, in order to characterize its pyrolysis kinetics, H_2S thermal decomposition into hydrogen and sulfur was studied in shock tubes [18–21] and tubular reactors [22,23]. Studies on oxidation are generally more recent, and were also performed in shock tubes [24,25], as well as flow reactors [26–29].

At a theoretical level, both pyrolysis and oxidation kinetics were investigated via targeted studies on the fundamental steps [20,30–32]. However, the number of kinetic mechanisms developed so far is quite limited. Frenklach et al. [24] developed a 17-species mechanism in order to model ignition delay time in shock-tube experiments, with variable amounts of H_2S and H_2O. Later, Sendt et al. [33] extensively used quantum chemistry calculations to build up a detailed kinetic mechanism of H_2S pyrolysis. They were followed by Zhou et al. [26,34], who extended such an analysis to oxidation, still leveraging fundamental calculations [35–38]. Bongartz and Ghoniem [39] developed a detailed chemical reaction mechanism for the oxy-fuel combustion of sour gas, thus including CH_4 chemistry and related interactions with sulfur species. To this purpose, they used the Zhou oxidation mechanism [26] to perform optimization, targeted to an experimental dataset made up of laminar flame speeds and flow reactor speciation. They found out that optimization alone was not sufficient to ensure accuracy in all the analyzed datasets, as matching the different experiments was competitive among each other. Therefore, they highlighted the need of more accurate experimental and theoretical data on sulfur kinetics. The newer work of Cong et al. [40] also extended the mechanism of Zhou et al. [26], specifically targeting the industrial production of hydrogen from H_2S pyrolysis and oxidation. Still in relationship to industrial processes, the state of the art of the kinetics of H_2S and sulfur-containing species was recently reviewed by Raj et al. [41].

In particular, very little is known, both experimentally and theoretically, about the reactivity of H_2S at low temperature and with high dilution levels. Furthermore, such conditions are of the utmost importance for the development of newer, more sustainable combustion concepts [42–44]. To the authors' knowledge, the only related experimental campaigns were carried out in the latest years by Song et al. [27] and Colom-Díaz et al. [11,28,29]. No data on H_2S pyrolysis were found below ~900 K, and as highlighted by Karan et al. [22], the extrapolation of the rate constants obtained via high-temperature data might result in significant deviations at lower temperatures. For oxidation, too, expanding the experimental database at lower temperatures, with variable oxygen amounts, would allow to shed more light on the reaction pathways governing oxidation kinetics, which can then be matter of further theoretical research.

In such scenario, this work aims at providing a more comprehensive insight on the pyrolysis and oxidation kinetics of H_2S at atmospheric pressure, under diluted conditions and over a wider range of temperatures, equivalence ratios and residence times. In order to cover such an operating space, three different experimental configurations were used, respectively a Jet-Stirred Reactor (JSR) and two Flow Reactors (FRs). In parallel, based on sensitivity analysis and literature review, the key rate constants involved in H_2S combustion chemistry were estimated through a first-principles approach. Finally, a detailed kinetic model of H_2S combustion was set up by both including the performed theoretical calculations and implementing the state-of-the-art kinetic rates involved in sulfur chemistry. This was leveraged to provide a deeper insight on the experimental results obtained in the different configurations, in both pyrolysis and oxidation conditions. Similarities and differences in the governing mechanisms in sulfur chemistry at high and low temperatures were thus highlighted, and the critical kinetic competitions, needing further theoretical research, were identified.

2. Methodology

2.1. Experimental setup

In order to explore a wide range of operating conditions, in terms of temperature (T), equivalence ratio (Φ), and residence time (τ), three different reactor facilities were adopted. All of them were operated at a near-atmospheric pressure (800 and 925 Torr), with helium as carrier gas. Diluted hydrogen sulfide (925 ± 2 ppm in helium) was provided by Messer. The purities of pure helium, needed to achieve the desired dilution, and of oxygen were 99.99%, and both of them were also provided by Messer. Flow rates were controlled using mass flow controllers purchased from Bronkhorst. The relative uncertainty in gas flow rates was about 0.5%. The explored experimental conditions are summarized in Table 1.

In a first setup, experiments were performed in a laboratory-scale fused silica JSR, a type of continuous stirred-tank reactor suitable for gas-phase kinetic studies. Its internal volume amounted to 85 cm^3, and it was operated at steady state. Such a setup is described in detail in previous works [45–47], thus a brief description is provided here. The reactor produced a high turbulence level thanks to four nozzles located at its center, thus leading to homogeneity in temperature and composition [48]. As a result, the JSR can be modeled as a perfectly stirred reactor. Inconel Thermocoax resistances rolled around the reactor were used to preheat and heat the JSR, and the reaction temperature was measured with a K-type thermocouple positioned in a glass finger close

Table 1
Summary of experimental conditions used in the present study.

Reactor	Material/Coating[a]	T [K]	P [Torr/kPa]	τ [s][b]	Φ [c] [-]	$x_{H_2S}^{inlet}$ [d] [ppm]
JSR	Fused silica / coated	500–1100	800/106.7	2	0.0184	500
					0.0367	
					0.25	
					∞	
					0.50	800
	Fused silica / non-coated	500–1100			∞	500
		400–1200			0.0184	
					0.0367	
					0.25	
					0.50	800
FR1	Alumina / coated	673–1273	950/126.7	0.1	0.25	500
				0.25	0.1	
		1073–1773			∞	
	Alumina / non-coated	973–1923		0.25	∞	
FR2	Alumina / coated	400–1200	800/106.7	2	0.25	500
		900–1600			∞	
	Alumina / non-coated	400–1200			0.25	
	Fused silica / coated					
	Fused silica / non-coated					

[a] the coating was performed at the laboratory using a boric acid solution (cfr. Section 2.1.1).
[b] the residence time is defined as the ratio between the reactor volume in the quasi-isothermal section and the gas flow rate (m^3/s) under the conditions of temperature and pressure in the reactor.
[c] the equivalence ratio was defined by considering the following stoichiometric equation: $H_2S + 1.5\ O_2 \rightarrow SO_2 + H_2O$.
[d] the diluent used in experiments was helium.

to its center (uncertainty of ± 5 K). Hydrogen sulfide pyrolysis and oxidation experiments were performed at a residence time of about 2 s and at temperatures ranging from 500 to 1100 K with initial fuel mole fractions of 500 and 800 ppm. Some experiments have been repeated twice providing an excellent reproducibility of the data (see Figure S11).

The second setup consisted of a flow reactor (identified as FR1) with an inner diameter of 4 mm and a length of 100 cm. It was located horizontally in an electrically heated oven (Carbolite Gero, working up to ~2000 K). An R-type thermocouple was used to measure temperature profiles (provided in the Supplementary Material). The isothermal reaction zone was located between 36 and 58 cm with a uniform temperature profile (±30 K). For each experiment, different residence times were studied and fixed constant to about 0.1 and 0.25 s, with initial fuel mole fraction of 500 ppm (thus the flow rates were adjusted for each experiment in order to keep a constant residence time). Flow rate conditions are also provided in the Supplementary Material.

The third setup used to investigate the pyrolysis and oxidation of H_2S at low-to-high temperatures (400–1600 K) was a flow reactor (identified as FR2). It worked under conditions close to those in the JSR facility (residence time of about 2 s), but also allowing experiments at higher temperatures. Different reactor materials were selected to investigate possible catalytic wall effects. For this reason, the reactor consisted in either a recrystallized alumina tube or a fused silica tube with an inner diameter of 20 mm and an external diameter of 25 mm. The total length of the tube was 60 cm. These tubes were purchased from SCERAM and can be used up to 1200 and 2000 K, for fused silica and alumina, respectively. The tube was located horizontally in a furnace (Vecstar). The oven had an internal temperature control, but the actual temperature profile was nevertheless measured using a shielded type S thermocouple with a diameter of 1 mm (temperature profiles are provided in the Supplementary Material). Such a thermocouple can withstand temperatures up to 1850 K. The isothermal reaction zone was located between 20 and 35 cm with a uniform temperature profile (±40 K), i.e., the nominal temperature. Flow rates used for each experiment are also given in Supplementary Material, as well as the atomic balances between inlet and outlet. Both FR1 and FR2 were designed to approximate plug-flow conditions (i.e. perfect segregation, with Peclet number > 50 [46,47]). The wall treatment performed to avoid catalytic effect and the analytical methods are described in Sections 2.1.1 and 2.1.2.

2.1.1. Wall treatment

Catalytic effects of the reactor wall altering H_2S reactivity were first observed in the fused-silica JSR, particularly during H_2S oxidation. Actually, the occurrence of wall catalytic effects had already been reported by other authors for the oxidation of the same fuel [26,49].

In order to prevent this, all the three types of reactor were treated with a solution of boric acid (boric acid in 50% water – 50% ethanol) to form an impervious layer of boric oxide, following recommendations by Zhou et al. [26], who had observed the enhancing effects of silica surface on H_2S oxidation. On the other hand, previous works [49–52] showed that boric acid is actually inert to the decomposition of peroxy species.

The main features of the coating procedure used in the present study are given hereafter (further details are given in the Supplementary Material). The vessel was first filled with a saturated solution of boric acid, then it was drained and dried with helium flowing through. The

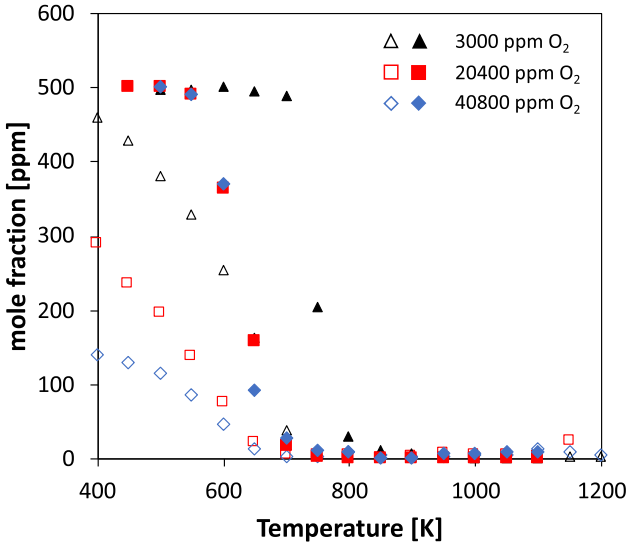

Fig. 1. Effect of coating on H_2S conversion: comparison between JSR without coating (void symbols) and with coating (filled symbols).

vessel was then heated to ~120 °C to eliminate the remaining solvent molecules. To obtain the impervious layer covering the wall, heating at 500 °C was needed. The obtained layer had a white color; it was translucent before the heating, while it became invisible after it, as mentioned in literature [26]. The procedure was repeated twice for the fused silica jet-stirred reactor due to a more complex geometry than in the tubular ones. Fig. 1 shows the effects of coating on H_2S conversion in the JSR: the importance of catalytic effects was found to be increasing with the amount of oxygen, with an earlier reactivity onset > 200 K. Such effects are qualitatively comparable with those observed by Zhou et al. [26] in their flow reactor, causing an earlier reactivity onset and a less steep conversion rate with the temperature.

2.1.2. Analytical method

On-line mass-spectrometry (MS) was used for the quantification of H_2S, H_2, H_2O, SO_2 and O_2. Sampling was achieved through a capillary tube directly connecting the reactor outlet and the analyzer. This technique requires the calibration of each species as there is no obvious relationship between their structures and their calibration factors. Gaseous standards were used except for water, which was calibrated considering the reaction complete at the highest temperature. Relative uncertainties in mole fractions of calibrated species detected by on-line mass spectrometry are ±10% (±20% for water).

H_2 was quantified using two techniques: online mass spectrometry and gas chromatography to validate the mass spectrometry detection method. The gas chromatograph (GC) used for H_2 quantification was equipped with a Carbosphere packed column providing a separation of the He and H_2 peaks. The detector was a thermal conductivity one and the carrier and reference gases were both Ar. The calibration was performed using a gaseous standard provided by Air Liquide. The relative uncertainty in H_2 mole fractions was estimated to be ±5% with this technique. GC and MS data were found to be in excellent agreement.

2.2. Theoretical methodologies

The rate constants for the H-atom abstractions by H, OH and O_2 from H_2S and of the recombination between SH and HO_2 were computed theoretically using EStokTP automatized routines [53] (available at https://github.com/EStokTP/EStokTP), which rely on Gaussian G09 [54] and Molpro 2021 [55] for electronic structure calculations, and MESS [56] (available at https://github.com/Auto-Mech/MESS) for Master Equation (ME) simulations.

Geometry optimization and frequency calculations of the stationary points of the Potential Energy Surfaces (PESs) were conducted at DFT level using B2PLYPD3 functional [57] and aug-cc-pVTZ basis set [58]. For H-atom abstraction reactions, also entrance and exit Van der Waals complexes were determined. The energies of all stationary points were refined at CCSD(T)/aug-cc-pVTZ level. Basis set size effects were accounted for by adding the energy difference at DF-MP2 level of theory computed with aug-cc-pVQZ and aug-cc-pVTZ basis sets. Instead, for the transition state (TS) of the H-atom abstraction by O_2, the high T1 diagnostics (0.08) indicated that multi-reference (MR) methodologies are required for a proper description of the energetics. Hence, the energy along the minimum energy path (MEP) was refined at CASPT2 (20e,14o)/aug-cc-pVTZ level of theory, using a level shift of 0.2. The reference CASSCF(20e,14o) wavefunction was equally weighted over the two lowest states. The energy was calculated with respect to the products SH + HO_2 at large separations (10 Å), and was then rescaled with respect to the reaction energy calculated at CCSD(T)/CBS level ($\Delta E_{TS,CASPT2} = \Delta E_{R,CCSD(T)} + (E_{TS,CASPT2}\text{-}E_{SH+HO2,CASPT2})$). Similarly, the MEP of SH + HO_2 association reaction to form HSOOH adduct was studied at CASPT2(20e,14o)/aug-cc-pVTZ//B2PLYPD3/aug-cc-pVTZ level, spanning a S-O distance of 2.4–10 Å. The energies along the MEP were also calculated with multireference configuration interaction (MRCI) including Davidson corrections [59,60] using the smaller cc-pVDZ basis set.

EStokTP also implements the treatment of internal rotations. Torsional potentials were computed at the same level of theory used for geometry optimization of the stationary points, with scans of 20° intervals. The corresponding partition functions were calculated using the one-dimensional hindered rotor (1DHR) model. To both verify the investigated reaction paths and to implement variational transition state theory (VTST), intrinsic reaction coordinate (IRC) calculations were performed considering 10–20 steps of 0.02 Å towards both reactants and products, and frequency analysis was conducted at each point.

The rate constants of the investigated reactions were computed in the 300–2500 K temperature range. All MESS input files are provided in the SM. The rate constants for H-atom abstraction reactions were computed with microcanonical VTST, as implemented in MESS [61]. Tunneling corrections were accounted for using the Eckart model [62]. As expected, the computed rate constants show no significant pressure dependence, hence in this work only the high-pressure limit rates are reported.

HO_2 + SH recombination to form HSOOH was treated with variable reaction coordinate TST (VRC-TST) [63,64] employing the 2TS methodology [65], as recently implemented in EStokTP. The reactive flux was evaluated over a multifaceted dividing surface [66]. Pivot points were placed at S and O atoms for the inner TS, and at the center of mass of the fragments at larger separations. A dynamical correction of 0.9 was included, as estimated from trajectory simulations on small systems [67]. The sampling of the orientations of the fragments was performed at CASPT2(4e,3o)/cc-pVDZ level, using fixed fragments geometries optimized at DFT level. The energies thus obtained were corrected with a S-O distance-dependent potential to account for both geometry relaxation and active space and basis set extrapolations. The former correction was obtained by constrained geometry optimizations at B2PLYPD3/aug-cc-pVTZ level, where only the relative orientation of the two fragments was optimized. The latter was instead derived as the difference between CASPT2(20e,14o)/aug-cc-pVTZ and CASPT2 (4e,3o)/cc-pVDZ energies calculated on the optimized geometries along the MEP. This correction was significant (above 1 kcal/mol) only at short S-O separations, namely below 2.6 Å. As noted in a previous work [34], HSOOH stabilization is negligible as its rapid dissociation to HSO + OH is orders of magnitude faster than its backward dissociation to SH + HO_2. In this work, the exit channel to HSO + OH was fictitiously included in the calculations using phase space theory. As a result, the final rate constant SH + HO_2 → OH + HSO (physically) corresponds to the high-pressure limit rate of the association reaction.

2.3. Kinetic modeling

The kinetic modeling of H_2S pyrolysis and oxidation was carried out through a hierarchical and modular methodology, as implemented in the CRECK kinetic framework (https://creckmodeling.chem.polimi.it/) [68]. The most relevant reactions composing the model are summarized in Table 2.

The core H_2/O_2 mechanism was taken from the work of Metcalfe et al. [75]. Following the modularity principle, a sulfur sub-mechanism was integrated into the main framework. Thus, starting from pyrolysis, the pressure-dependent H_2S thermal decomposition (R1) was considered. As a matter of fact, the theoretical study of reaction R1 is not immediate. It involves both the barrierless decomposition to H_2 + S(1D) on the singlet PES and intersystem crossing (ISC) to the triplet PES leading to the formation of H_2 + S(3P), resulting in strong non-Arrhenius behavior. In addition, a complete study of such PES requires considering the competition between S(3P) + H_2 = H_2S and S(3P) + H_2 = SH + H, both occurring on the triplet PES. All channels are also expected to show a significant pressure dependence. Therefore, theoretical studies on R1 are pretty scarce. To the authors knowledge, the only available theoretical works were performed by Shiina et al. [20,76]. Fig. 2 compares the kinetic rates proposed for R1 by different authors [18–20,22,76], as well as the few available experimental data [18,19,22]. They differ even

Table 2
List of key reactions in the H_2S pyrolysis and oxidation mechanism. Reaction rate expression is modified Arrhenius. $k = AT^{\beta} \exp[-E_{act}/(RT)]$. Units are cm^3, s, cal, mol, K. The adjustments performed to the calculated parameters or literature ones are reported in 'Notes'. PW = Present Work. CHEMKIN keywords are adopted.

ID	Reaction	A	β	E_{act}	Notes	Ref
R1	$H_2S + M = H_2 + S + M$	5.10×10^{13}	0.000	56140		[22]
R2	$SH + O_2 = HSO + O$	2.30×10^{6}	1.816	20008		[37]
R3	$SH + O_2 = S + HO_2$	4.70×10^{6}	2.017	36913		[37]
R4	$SH + O_2 = SO + OH$	7.50×10^{4}	2.100	16384		[37]
R5	$SH + O_2 = SO_2 + H$	1.50×10^{5}	2.123	11020		[27]
R6	$SH + HO_2 = H_2S + O_2$	4.62×10^{6}	1.921	−1500	A × 2.5; E_{act} − 1000	PW
R7	$SH + HO_2 = HSO + OH$	5.17×10^{12}	0.134	−807	E_{act} −500	PW
R8	$H_2S + O = SH + OH$	1.86×10^{5}	2.644	2032	E_{act} −500	[69]
R9	$H_2S + H = SH + H_2$	8.87×10^{8}	1.517	2051	A × 0.67	PW
R10	$H_2S + OH = SH + H_2O$	1.63×10^{7}	1.851	−491		PW
R11	$SH + H_2O_2 = H_2S + HO_2$	5.60×10^{4}	2.823	8668		[34]
R12	$SH + H_2O_2 = HSOH + OH$	9.49×10^{3}	2.800	9829		[34]
R13	$H_2S + SO = SH + HOS$	1.00×10^{13}	0.000	36500		[26]
R14	$H_2S + SO = SH + HSO$	5.38×10^{3}	3.200	26824		[26]
R15	$H_2S + S = SH + SH$	7.49×10^{13}	0.000	7390	A × 0.9	[20]
R16	$S + O_2 = SO + O$	5.43×10^{5}	2.100	−1451		[70]
R17	$SO + O_2 = SO_2 + O$	8.91×10^{6}	1.400	3712		[71]
R18	$SH + S = S_2 + H$	3.31×10^{12}	0.500	−29		[34]
R19	$SH + HS_2 = H_2S + S_2$	6.27×10^{3}	3.050	−1105		[33]
R20	$SH + O = SO + H$	3.61×10^{11}	0.700	−1027	A × 0.85	[72]
R21	$S_2 + O = S + SO$	1.43×10^{11}	0.700	-231		[34]
R22	$SO_2 + H(+M) = HOSO(+M)$	2.32×10^{10}	0.960	8584		[73]
	LOW	2.10×10^{31}	−4.360	10809		
R23	$SO + OH(+M) = HOSO(+M)$	1.56×10^{12}	0.500	−400		[73]
	LOW	9.54×10^{27}	−3.480	970		
R24	$SO + O(+M) = SO_2(+M)$	3.20×10^{13}	0.000	0		[74]
	LOW N_2 / 1.5 / H_2O / 10 / SO_2 / 10 /	1.22×10^{21}	−1.540	0		

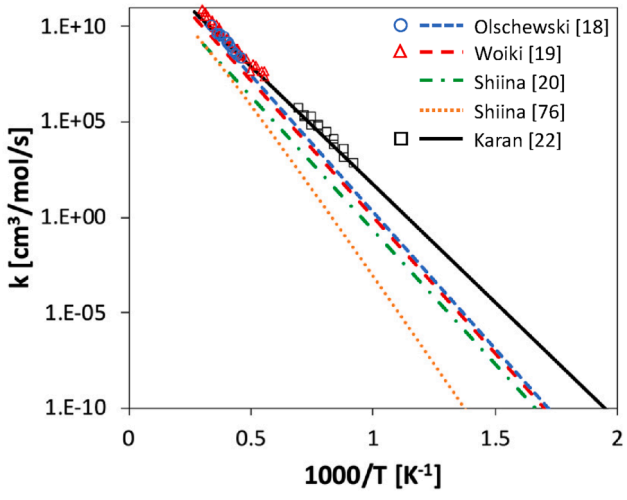

Fig. 2. Rate constants (lines) proposed for the thermal decomposition of H_2S (R1) by several sources [18–20,22,76], and related experimental data (symbols) [18,19,22].

by 4 to 5 orders of magnitude, especially at low temperatures (~1000 K). Moreover, except for the work of Karan et al. [22], most data were obtained at very high temperatures. In this work, the kinetic rate proposed in this last work [22] was chosen, as the result of an optimization among the different experimental datasets, and as shown in Fig. 2, it was proven the most accurate in reconciling low- and high-temperature data.

The pyrolysis subset for the H_2/S_2 system (SH, HSSH, HSS, S, S_2, H_2) was then completed with the submechanism proposed by Sendt et al. [33], later updated by the study of Zhou et al. [36].

Concerning the oxidation model, the oxidation reactions of the SH radical with O_2 were adopted after the work of Zhou et al. [37] on the related branching ratio, with R5 updated after the recent estimation of Song et al. [27]. Regarding reactions with HO_2, of possible importance in this activity due to the low-temperature conditions encountered, the branching ratio of the reaction of SH + HO_2, providing either a termination (R6) or a propagation (R7), was re-calculated from scratch as already illustrated in Section 3.1. H-abstractions were taken from the most updated sources, where theoretical estimations were performed; reaction with HO_2 was kept from the same previous reference [37]. The work of Wang et al. [69] was used instead for abstraction by O, while H-abstractions by H (R9) and OH (R10) were calculated as described in Section 3.1. For HO_2, the reverse rate (R11) was adopted, in competition with R12 providing instead HSOH + OH [34]. Regarding sulfur-containing species, abstractions by SO were taken from the

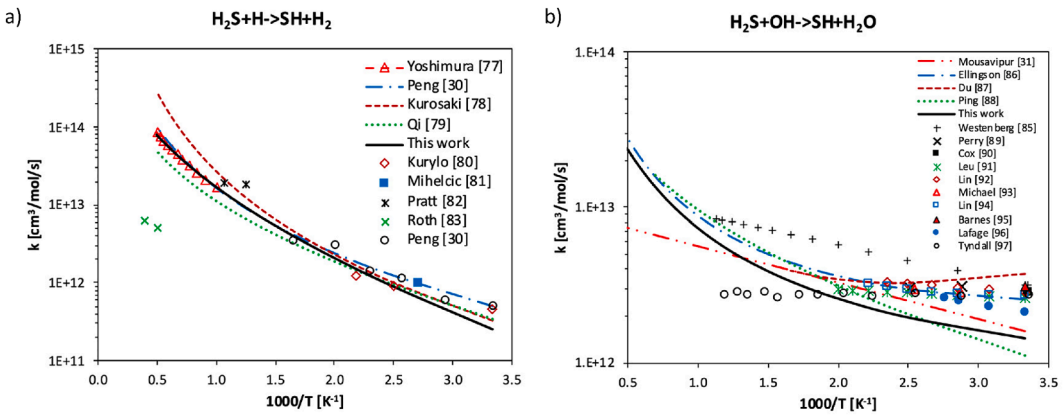

Fig. 3. Computed rate constants for the H-atom abstraction reactions by a) H and b) OH from H_2S in comparison with the available theoretical [30,31,77–79,86–88] and experimental [30,80–83,85,89–97] literature estimates.

estimations of Zhou et al. [26], included in their oxidation model, while for reaction with S (R15), the experimental data by Shiina et al. [20] were fitted through a three-parameters Arrhenius rate, and supposing a branching ratio equal to 90% of the channel providing two SH radicals. For some of the reactions (R6, R7, R8, R9, R15, R20), small modifications of the kinetic parameters were performed (still within their estimated uncertainty) for an improved agreement with the experimental data (the datasets obtained in this work as well as those available in literature).

3. Results and discussion

3.1. Evaluation of rate constants

Fig. 3a shows the computed rate constant for the H-atom abstraction reaction by H from H_2S in comparison with the available literature data [30,77–83]. The present calculations generally agree with experimental estimates, with the exception of the dataset of Roth et al [83]. Previous theoretical estimates obtained with different methodologies also support the theoretical accuracy of our result. In particular, we found less than 50% discrepancy with the recently calculated rate of Qi et al [79], who performed quantum dynamical calculations on the FC-UCCSD(T)-F12a/aug-cc-pVTZ PES derived by Lu et al [84]. The less recent CTST results of Peng et al. [30] are larger than the present calculated rate by a maximum factor of 2 at 300 K. However, their energy barrier of 3.82 kcal/mol computed at QCISD(T)/6–311 + G(3df,2p) level of theory was lowered to 3.44 kcal/mol for a better agreement with experimental data. Considering their calculated barrier of 3.82 kcal/mol leads instead to an increase in their rate constant by about a factor of 2 at 300 K and therefore to excellent agreement with the present calculations, which are expected to be more accurate at least in terms of the single point energy calculations at CCSD(T)/CBS level. Our calculated energy barrier of 3.2 kcal/mol corresponds instead to the corrected energy barrier of Yoshimura et al [77], who originally obtained 4.11 kcal/mol at PMP4 (SDTQ)6-311G(d,p)//MP2/6-31G(d,p) level. The largest discrepancies (factor of 3.5) with former theoretical estimates are found at high temperatures with the rate constant of Kurosaki et al [78], who performed VTST calculations on a PMP4(SDTQ,full)/cc-pVTZ//MP2(full)/cc-pVTZ PES. Such differences are reasonably within the uncertainties of the theoretical methodologies used.

The comparison between the calculated H-atom abstraction rate constant by OH from H_2S is found in Fig. 3b. With maximum differences

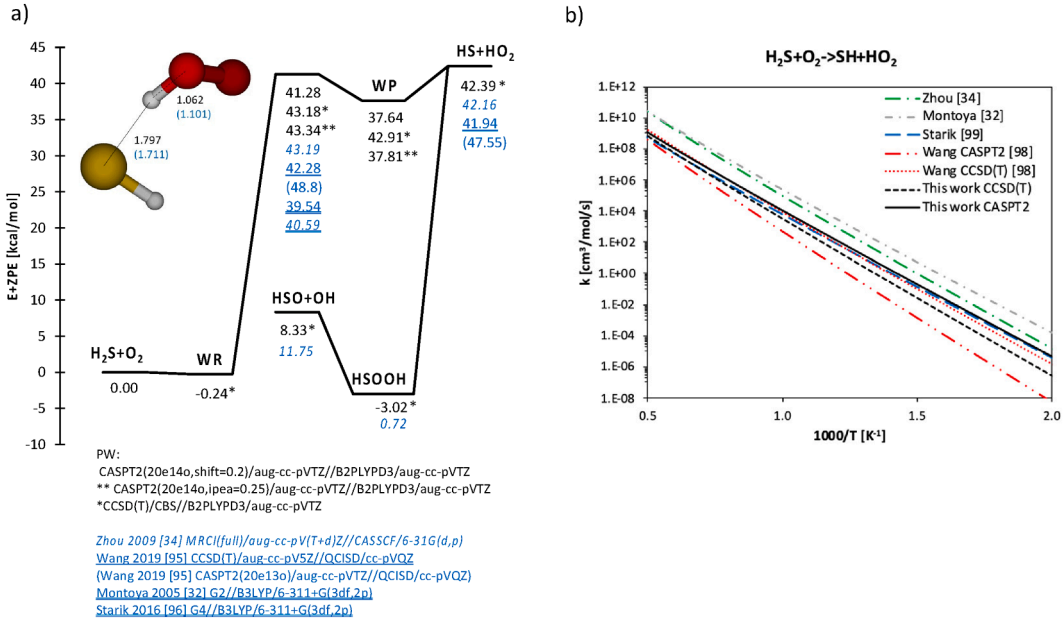

Fig. 4. a) Potential energy surface of the SH + HO_2 system and b) Computed rate constants for the H-atom abstraction reaction by O_2 from H_2S in comparison with the available theoretical literature estimates [32,34,98,99].

of a factor of 2.3 with respect to the experimental estimates of Westenber et al [85], our calculated rate generally agrees with the experimental data within a factor well below 1.8. The slight underestimation of most datasets at lower temperatures might be easily explained by assigning an uncertainty of 0.5 kcal/mol to the energy barrier of this reaction, which we computed as 0.7 kcal/mol at CCSD(T)/CBS level. A closer agreement at lower temperatures was in fact obtained by Ellingson and Truhlar [86], who calculated a M06-2X/MG3S barrier of −0.24 kcal/mol. A slightly higher value of 0.18 kcal/mol was instead obtained at CCSD(T)/6–311++G(3df,3pd)//BH&HLYP/6–311++G(3df,3pd) level by Zhang [87].

Larger disagreement is found among the literature data for the H-atom abstraction by O_2 from H_2S (Fig. 4b), showing maximum discrepancies up to 4 orders of magnitude in the 500–2000 K range. This is partially related to significant differences in the theoretical calculations of the energy barrier of this reaction, listed on the PES of Fig. 4a together with the corresponding theoretical methodologies employed. The PES also includes SH + HO_2 recombination pathway, discussed later in this section. The results of the present work for the energy barrier (ΔE_{TS}) and the reaction energy (ΔE_R) (41.28 and 42.39 kcal/mol, respectively), reasonably agree with previous works within 4 kcal/mol, with the exception of the MR values obtained by Wang et al. [98]. Their CCSD(T)/aug-cc-pV5Z//QCISD/cc-pVQZ barrier of 42.28 kcal/mol agrees with other works. Nevertheless, their high T1 diagnostics (0.04) suggested that MR treatment is necessary. Their CASPT2(20e,13o)/aug-cc-pVTZ//QCISD/cc-pVQZ ΔE_{TS} and ΔE_R dramatically increase from 42.28 and 41.94 to 47.55 and 48.80 kcal/mol, respectively. Such disagreement cannot be attributed to the TS structure, which is similar to that found in the present work (bond distances are compared in Fig. 4a).

Because our CASPT2(20e,14o)/aug-cc-pVTZ barrier was calculated relatively to SH + HO_2 and then rescaled with respect to the CCSD(T)/CBS reaction energy (see Section 2.2), the large difference with Wang calculations might be related to the energy of the reactants, which they used as reference. Therefore, we also calculated the ΔE_R at MR level, however obtaining 43.96 kcal/mol. The experimental ΔE_R of 41.32 kcal/mol estimated from NIST database (https://cccbdb.nist.gov/) supports the values obtained in this work. As expected, the large variations of the literature values in the ΔE_{TS} directly affect the corresponding rate constants (Fig. 4b). Nevertheless, they are still insufficient to fully account for the discrepancies found. For instance, Starik et al. [99] refined the energy barrier of Montoya et al. [32] from G2 to G4 level by 1 kcal/mol, however the resulting rate constant is more than one order of magnitude lower than that of the previous work. Starik et al. attributed this change to the treatment of internal rotations: their 1D hindered rotor treatment for the torsion of O_2 decreased the rate constant by a factor of ~5 with respect to the RRHO approximation used by Montoya et al. Similarly, in this work we found that 1DHR treatment of internal torsions for this TS lowers the rate by a factor of about 3–4. Our recommended CASPT2 rate closely agrees with the values calculated by Starik at al. [99].

The reactivity of SH + HO_2 and its branching between the backward H-abstraction reaction to H_2S + O_2 and the recombination channel leading to HSO + OH are essential to determine both low-temperature product distribution in oxidation conditions and H_2S ignition properties, as highlighted in Sections 3.2.2 and S1.1. The energetics of both channels is reported in Fig. 4a, whereas MEP mappings at the same level of theory are presented in Fig. 5a. It is noted that the H-atom abstraction reaction occurs on a triplet PES, whereas energies for the recombination channel were computed on the singlet PES. The singlet–triplet splitting at large separations (~above 3 Å) is estimated to be negligible. As far as SH + HO_2 → H_2S + O_2 is concerned, our CASPT2(20e,14o)/aug-cc-pVTZ barrier is estimated to be 1.1 kcal/mol below SH + HO_2 (Fig. 4a). However, the IRC mapping (red axis and curve of Fig. 5a) resulted in a small positive barrier of 0.66 kcal/mol. The non-Arrhenius temperature dependence at lower temperatures (Fig. 5b) is mostly attributed to tunneling corrections, which increase the rate constant up to a factor of 10 at 300 K due to the deep Van der Waals complex (WP in Fig. 4a and local minimum in Fig. 5a). This well was neglected by Zhou [34], who in fact reported a stronger Arrhenius T-dependence in their rate constant, also caused by their higher activation energy. Their larger values at high temperatures are instead mostly due to their RRHO treatment for the TS internal torsion, as highlighted above. Interestingly, the exit Van der Waals complex of the backward H-atom abstraction reaction is almost identical to the complex found along the MEP of SH + HO_2 recombination (black solid line in Fig. 5a).

Similarly to Zhou [34], we found a local minimum at about 3.4 Å S-O separation, and a local maximum at about 3.0 Å. The calculated CASPT2 energies generally agree within 0.5–1 kcal/mol with our calculated MRCI(20e,14o) + Davidson/cc-pVDZ energies. As expected, differences of 1–1.5 kcal/mol are found at shorter separations (2.5–2.6 Å), however the minimum reaction flux was reached only at larger distances (above 3 Å). The rate constant obtained shows almost no temperature

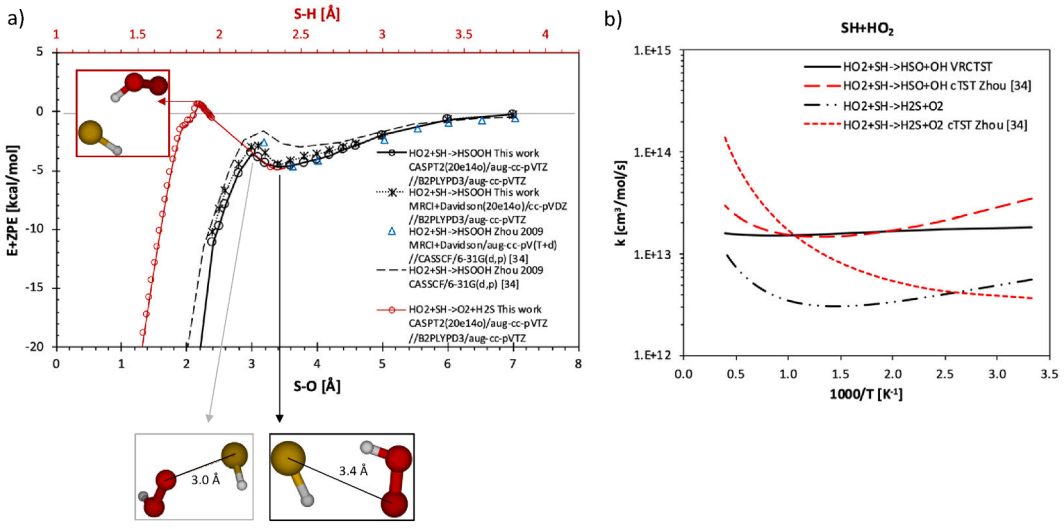

Fig. 5. a) Minimum energy path and b) rate constants for the HO_2 + SH reaction producing H_2S + O_2 and HSOOH in comparison with the available literature data [34]. In figure a), the upper red x-axis indicates the S-H distance used for mapping the backward H-abstraction reaction. The local minimum common to both MEPs correspond to the same well structure, obtained independently on the singlet and triplet surfaces. (For interpretation of the references to color in this figure legend, the reader is referred to the web version of this article.)

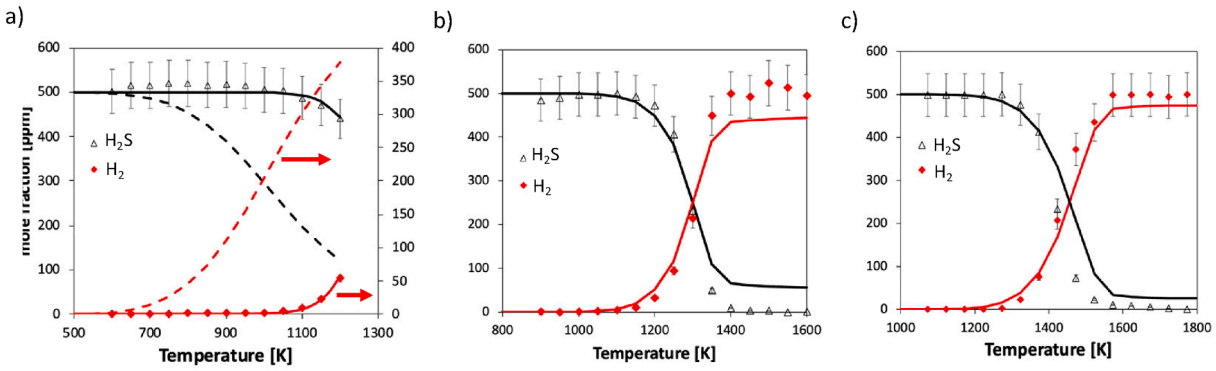

Fig. 6. Pyrolysis of 500 ppm H_2S in ideal reactors. a) JSR ($\tau = 2$ s – P = 800 Torr). b) FR2 ($\tau = 2$ s – P = 800 Torr). c) FR1 ($\tau = 0.25$ s – P = 925 Torr). Experimental (symbols) and modeling (lines) results. Dashed lines (panel a) indicate equilibrium mole fractions.

dependence with a value of ~1.5E+13 cm^3/mol/s. The present calculations are in good agreement with the previous CTST estimate of Zhou (within a factor of 2) [34]. However, the competition between the recombination and abstraction channels differ substantially from the predictions of Zhou [34]. In fact, in the present results the SH + HO_2 → H_2S + O_2 channel never predominates, although it contributes significantly to the total rate constant by about 20–40%. On the contrary, Zhou obtained that at higher temperatures the SH + HO_2 → H_2S + O_2 channel largely prevails over the recombination. The tuning of the kinetic model in the present work led to changing the branching fraction of the SH + HO_2 → H_2S + O_2 channel to 40–60% for better agreement with the experimental data (see R6, R7 in Table 2). The adjustment of the SH + HO_2 → H_2S + O_2 activation energy by 1 kcal/mol is consistent with the estimated uncertainties of the present theoretical calculations.

3.2. Experimental results and kinetic modeling

The combustion behavior of H_2S was experimentally investigated by following a hierarchical methodology. As shown in Table 1, in all of the three reactors, pyrolysis experiments were first carried out, and the availability of different experimental configurations allowed to explore the widest possible temperature (T) range, and accordingly residence times (τ). Afterwards, oxidation campaigns were performed with the same approach: in this case, in addition to variable T and τ, the effect of the progressive oxygen addition and H_2S amount was also analyzed. All data sets are provided under the form of spreadsheets in Supplementary Material.

The use of the kinetic model allowed to interpret the experimental data, and to explain H_2S conversion throughout the full range of operating conditions. A wider-range validation of the kinetic mechanism against ignition delay time, laminar flame speed, flow and jet-stirred reactors is provided in the Supplementary Material (Section S1).

3.2.1. Pyrolysis

After coating the three reactors, pyrolysis experiments were performed in each of them, by using 500 ppm H_2S in a helium atmosphere. Results are shown in Fig. 6 for both H_2S and H_2 mole fractions. For Fig. 6a, equilibrium data are also added, and point out that the system is kinetically governed, far from equilibrium conditions. In the JSR, no fuel consumption can be observed before ~1000 K, and the final conversion at the maximum allowed temperature (1200 K, due to the mechanical resistance of the quartz material) is slightly higher than 10%. On the other hand, complete conversion can be observed at high temperatures in FR2 and FR1, where a 50% conversion is reached for T = 1300 K and T = 1450 K, respectively (mostly due to the different residence times). The kinetic model is able to reasonably predict the fuel consumption, in terms of both reactivity onset and conversion rate with temperature. At higher temperatures, a residual presence of H_2S is predicted by the kinetic model, whilst not observed experimentally. This is due to the quenching section of both reactors, where the lower temperatures shift the equilibrium from H_2 and S_2 to H_2S, thus bringing to product recombination. This is not observed experimentally, though, and could be likely due to the deposition of sulfur in the cold part of the reactor at its outlet, preventing further reaction with H_2. Solid matter was indeed collected afterwards when cleaning the tube of FR1 reactor (cfr. Figure S10 in the Supplementary Material).

The fate of sulfur atoms from H_2S to the diatomic S_2 was numerically analyzed via reaction flux analysis, performed in the case of maximum conversion obtained in the JSR (~10% at T = 1200 K). This is shown in Fig. 7a, and highlights a double pathway leading to S_2 formation. This occurs either via the thermal decomposition of the fuel (R1), or via H-abstraction by H atom (R9), providing SH, on turn converted to S_2 via

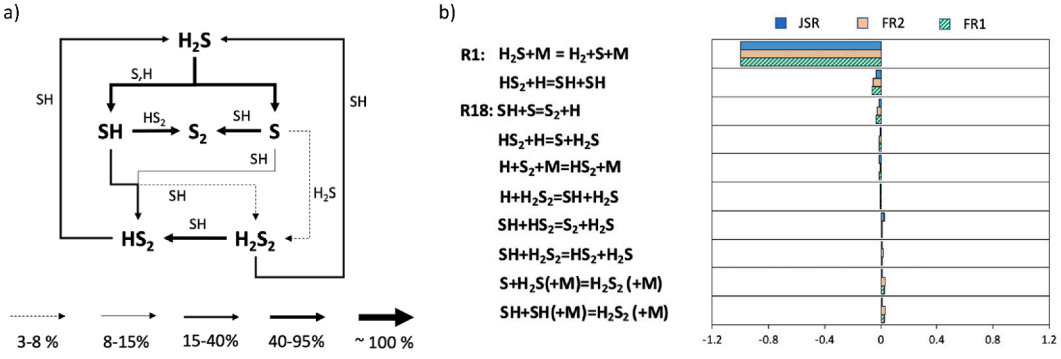

Fig. 7. a) Sulphur flux analysis in the pyrolysis of 500 ppm H_2S in JSR (T = 1200 K). Flux intensity is related to the single molecule. b) Sensitivity analysis to H_2S mass fraction (normalized with respect to the maximum value) in the 3 configurations, for ~10% H_2S conversion. For FR1 and FR2, 50% reactor length was chosen for such evaluation.

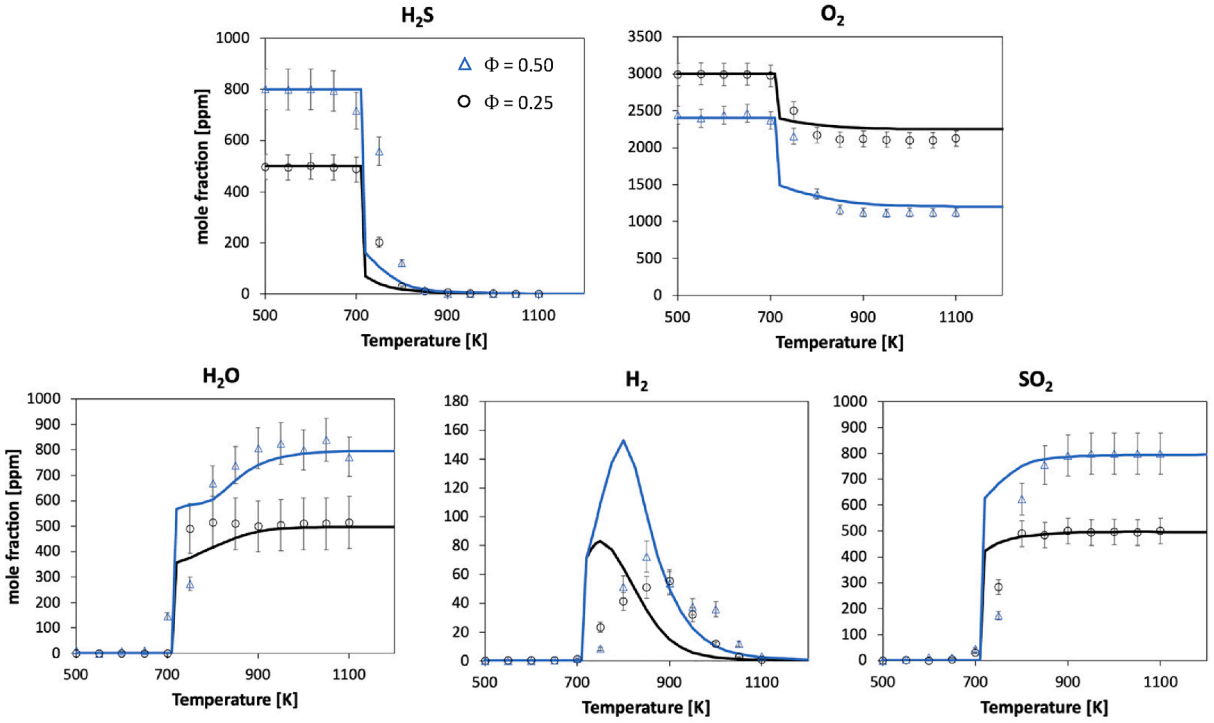

Fig. 8. Oxidation of 500 ppm (Φ = 0.25) and 800 ppm (Φ = 0.50) H_2S in a Jet-Stirred Reactor (τ = 2 s, P = 800 Torr). Experimental (symbols) and modeling (lines) results.

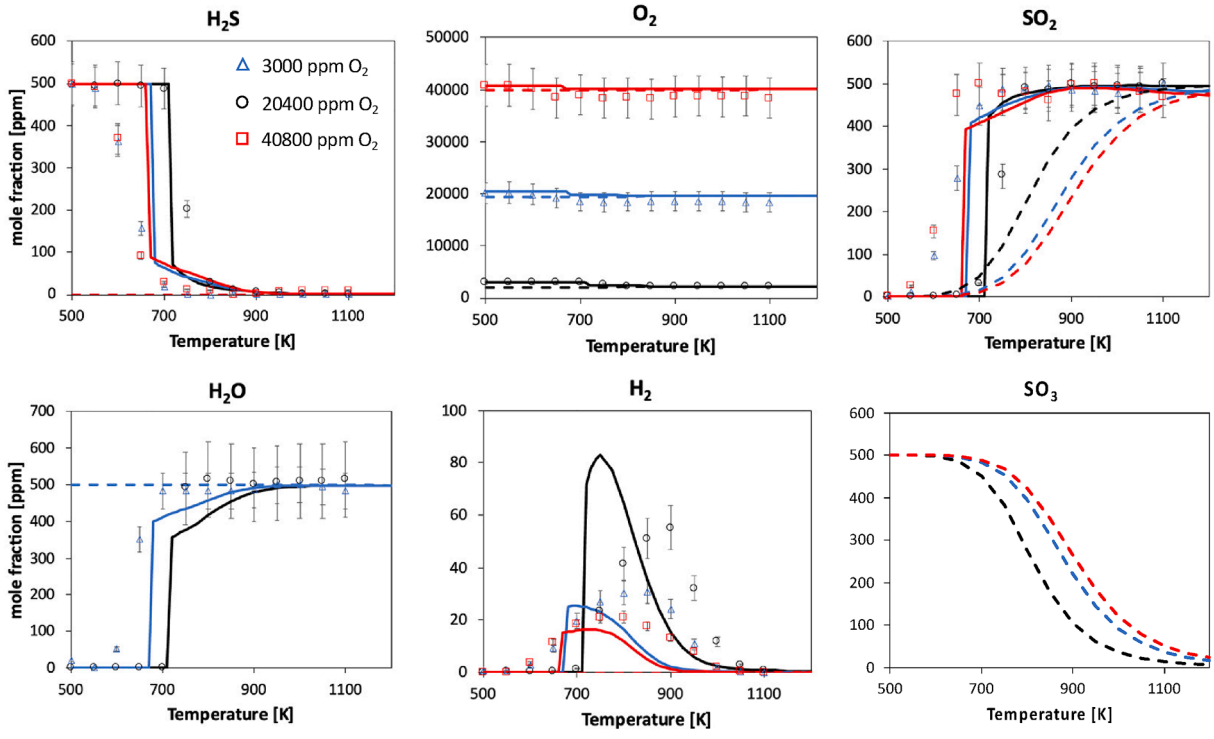

Fig. 9. Oxidation of 500 ppm H_2S in a Jet-Stirred Reactor (τ = 2 s, P = 800 Torr) with variable amounts of O_2. Experimental (symbols) and modeling (lines) results. Dashed lines indicate equilibrium mole fractions.

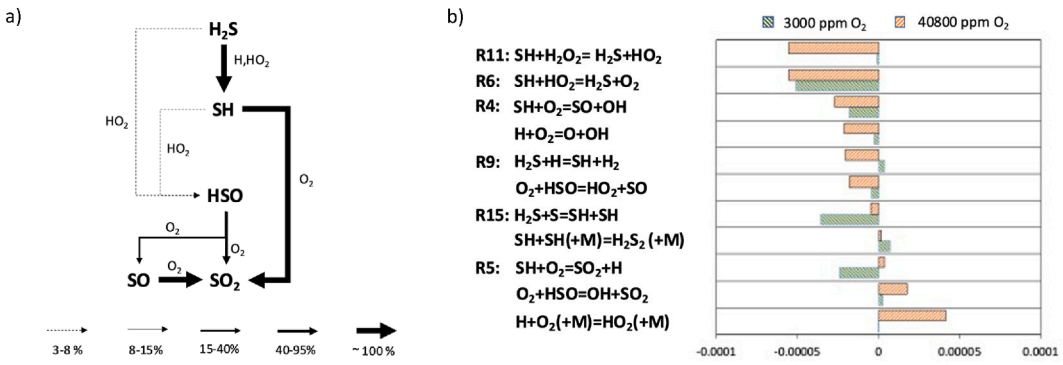

Fig. 10. a) Sulfur flux analysis in the oxidation of 500 ppm H_2S with 40800 ppm O_2 in a JSR. T = 650 K. b) Sensitivity analysis to H_2S mass fraction with 3000 ppm O_2 (T = 700 K) and 40800 ppm O_2 (T = 650 K), respectively. τ = 2 s. P = 800 Torr.

either S or HS_2. Nevertheless, the controlling step of the whole pyrolysis process is R1 regardless of the operating temperature, as shown by the sensitivity analysis (Fig. 7b) performed in each of the three reactors, for a final 10% H_2S conversion. As soon as S radicals become available, SH are generated via H-abstraction (R9, R15), and this ultimately brings to S_2 via S (R18) and HS_2 (R19).

3.2.2. Oxidation

At lower temperatures, the oxidation of hydrogen sulfide was studied in the JSR by considering 800 ppm H_2S as inlet fuel under lean conditions ($\Phi = 0.50$), and 500 ppm H_2S under very lean conditions ($\Phi = 0.25$ and below), with an increasing amount of oxygen up to 40800 ppm. Results are shown in Fig. 8 and Fig. 9, and report the profiles of reactants (H_2S, O_2), major products (SO_2, H_2O) and H_2 as intermediate species. In Fig. 9, equilibrium data are also plotted, and show also in this case that the system is kinetically driven, far from equilibrium. No H_2 is expected to be formed, in significant amounts, in equilibrium conditions, while especially at low temperatures the amount of SO_2 in equilibrium conditions is much lower than the actual one. This is because at low temperatures, and equilibrium conditions, sulfur is mostly oxidized to SO_3, which is shown in Fig. 9, too, for the sake of completeness (only equilibrium, since no SO_3 is actually experimentally detected, or predicted by the kinetic model). With the lowest oxygen amounts, an abrupt onset of the reactivity can be observed, and most of the fuel (~80%) is consumed over a temperature interval of ~50 K. Such an interval becomes wider with higher oxygen amounts, up to ~150 K in the leanest conditions (40800 ppm O_2). On the other hand, the kinetic model predicts a steep conversion rate with temperature, regardless of the oxygen amount. In all of the cases, 80% of the fuel is predicted to be consumed in less than 20 K. In addition to chemistry, the reason behind this discrepancy in the JSR can also be attributed to the presence of residual wall effects, persisting even after the coating operation. As shown in Fig. 1, such effects are indeed strongly emphasized by the incremental presence of oxygen. Overall, the onset temperature is predicted reasonably well for the two highest equivalence ratios, while a slightly delayed onset (~50 K) is present with 20400 ppm and 40800 ppm O_2.

In order to shed light on the chemistry triggering the reactivity onset at the lowest temperatures, Fig. 10a shows the reaction flux analysis,

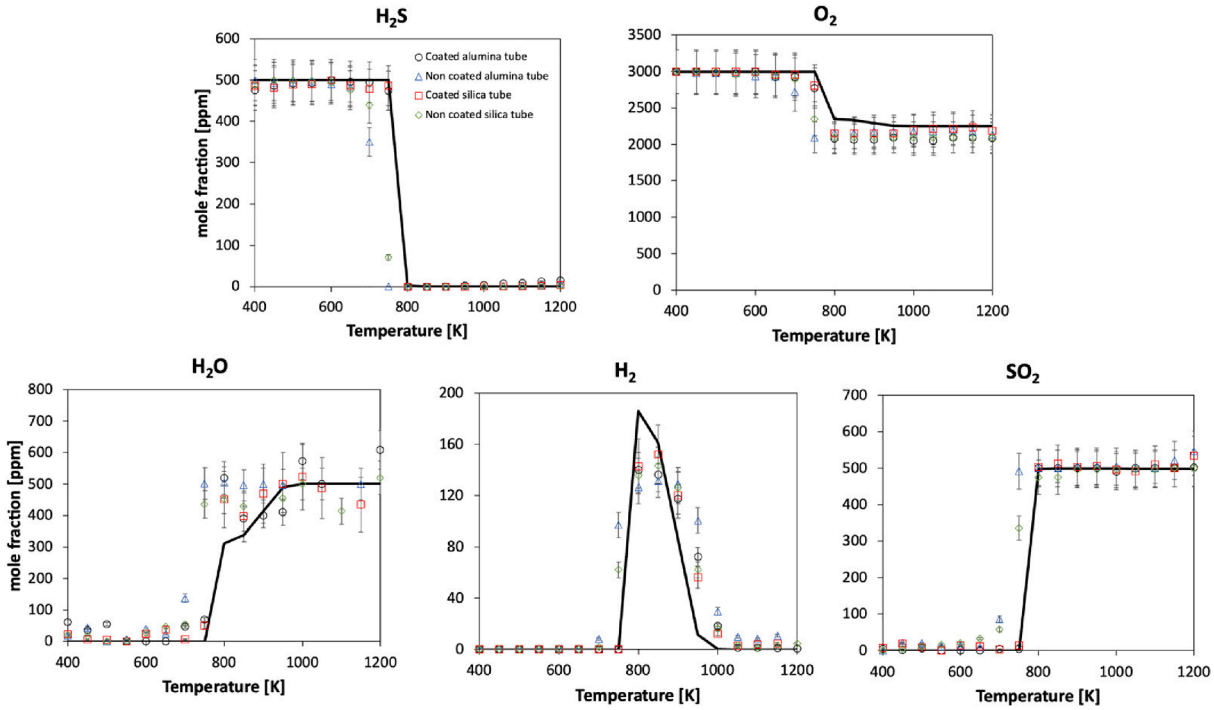

Fig. 11. Oxidation of 500 ppm H_2S with 3000 ppm O_2 (Φ = 0.25) in a flow reactor (FR2), with different reactor material and coating. τ = 2 s. P = 800 Torr. Experimental (symbols) and modeling (lines) results.

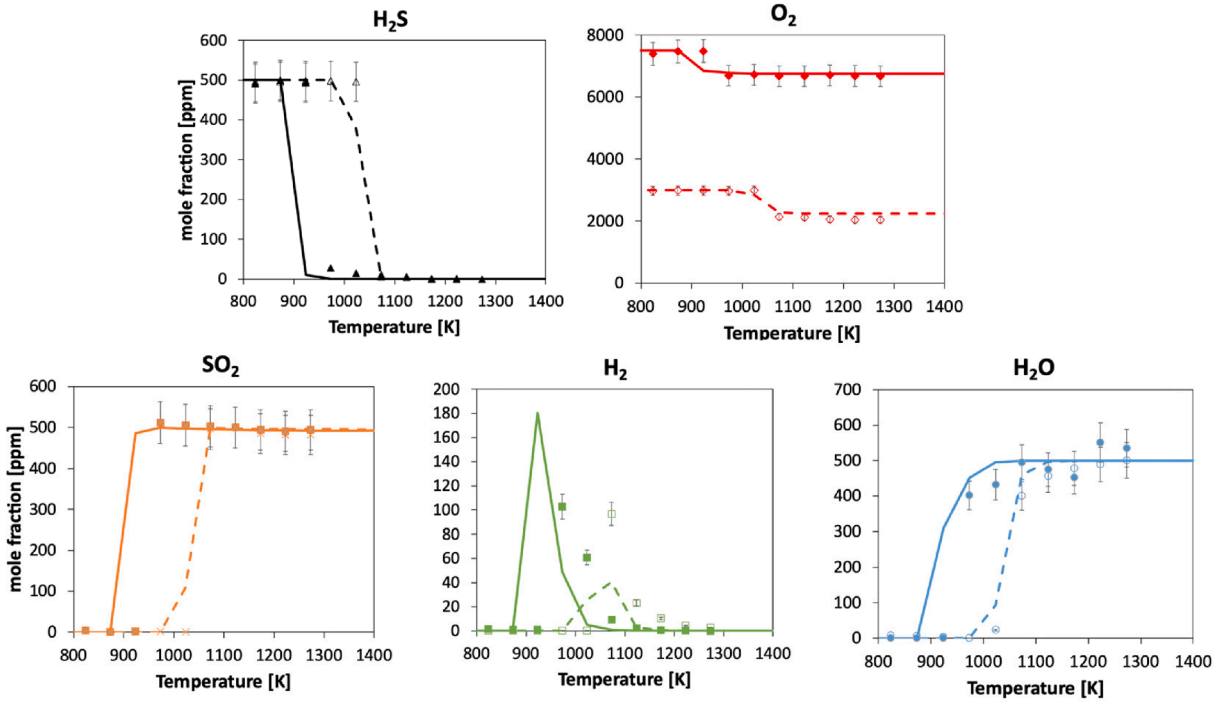

Fig. 12. Oxidation of 500 ppm H_2S in a flow reactor (FR1). P = 800 Torr. Full symbols and continuous lines: $\Phi = 0.1$, $\tau = 0.25$ s. Open symbols and dashed lines: $\Phi = 0.25$, $\tau = 0.1$ s. Experimental (symbols) and modeling (lines) results.

based on the S atom, performed in the leanest conditions, at a temperature preceding the start of fuel consumption. At the same time, the sensitivity analysis illustrated in Fig. 10b complements such information by highlighting the reaction steps actually triggering the reaction. The combined analysis of both figures shows that in this case, too, the availability of SH radicals drives the start of fuel consumption, since radical branching is then activated via R4 and R5. Furthermore, under lean and very lean conditions, the critical SH radical pool is built up differently: as shown in Fig. 10b, with 3000 ppm O_2 the process is controlled by the H-abstraction on H_2S by O_2 (R6b), i.e. the dominating source of SH radicals. On the other hand, in very lean conditions (40800 ppm O_2), the large amount of HO_2 obtained via R6b because of a higher O_2 availability allows the further H-abstraction on H_2S by HO_2 itself via R11b, further increasing the SH radical pool. At the same time, the higher amount of O_2 also enhances the third-body reaction with H radical via $H + O_2(+M) = HO_2(+M)$, with an opposing effect on reactivity. Conversely, H-abstraction by the H atom (R9) enhances the growth of SH radical pool, and subtracts H radicals to the mentioned third-body reaction with O_2. The net result is an anticipation of the onset temperature, as already shown in Fig. 9.

Subsequently, H_2S oxidation under lean conditions ($\Phi = 0.1$ and 0.25) was investigated in the two flow reactors. In this case, the different residence times in FR2 and FR1 allowed to explore intermediate- and high-temperature conditions, respectively. Regarding FR2, Fig. 11 shows the profiles of the major species by using two different materials for the reactors (alumina and silica), before and after performing the coating procedure (cfr. Section 2.1.1) for both of them. Compared to JSR (Fig. 1), the effect of coating on H_2S conversion is much less evident in this configuration, and after treating the wall the reactivity onset is delayed by only 50 K for both alumina and silica tubes. In addition to this, the conversion rate with temperature is much steeper in this case with respect to the perfectly stirred conditions (see Figure S3), and differently from the previous case, no residual presence of the fuel can be observed right after ignition is triggered. In general, a good agreement can be observed between the predictions of the kinetic model and the data of all the species obtained with the coated tubes. As in the case of

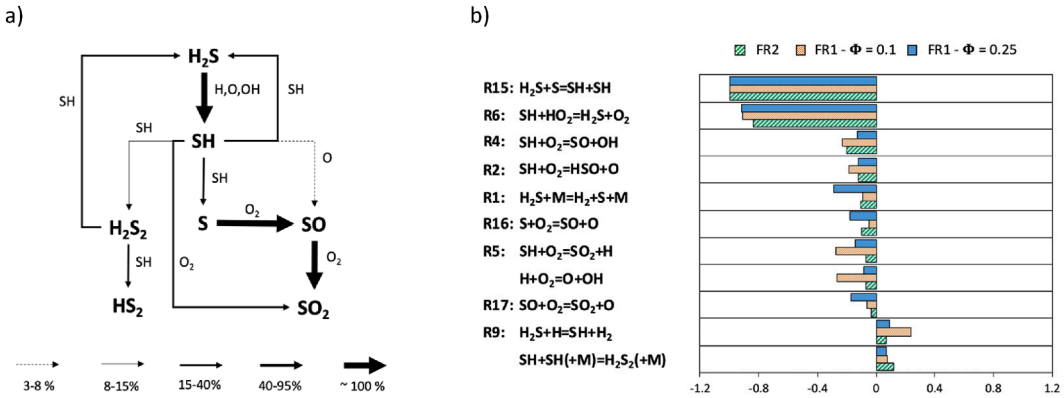

Fig. 13. a) Sulfur flux analysis in the oxidation of 500 ppm H_2S in FR1. $\Phi = 0.1$, $\tau = 0.25$ s. b) Sensitivity analysis to H_2S mass fraction (normalized with respect to the maximum value) in the 3 oxidation datasets for FR1 and FR2, in correspondence of H_2 peak. The reactor coordinate where 1% H_2S conversion was achieved was chosen for such evaluation.

the JSR data (Fig. 8 and Fig. 9), the H_2O profile exhibits a double inflection point, and this is due to the formation of H_2 in the 800 K – 1000 K window, which is also well reproduced by the numerical simulations.

Finally, the oxidation was studied at higher temperatures in FR1, whose residence time is $\tau = 0.1$ s – 0.25 s, i.e. one order of magnitude lower than FR2 ($\tau = 2$ s). Fig. 12 shows the speciation profiles of the major species for two different initial conditions, in terms of equivalence ratio ($\Phi = 0.25$ and $\Phi = 0.1$), for which the residence time was adjusted accordingly ($\tau = 0.1$ s and $\tau = 0.25$ s, respectively). Alumina was the only material considered in this case, and only coated data are shown here.

Results show a similar qualitative behavior for the two datasets, with the only macroscopic difference being the onset temperature: under the leanest conditions, the mixture starts reacting at a temperature 100 K lower. In this case, the experimental trends are also reproduced fairly well by the kinetic model, with a slight underprediction of the onset temperature (50 K).

In order to understand the differences in the controlling reaction steps, with respect to what is observed at lower temperatures, in perfectly stirred conditions, reaction flux analysis was performed for a sample condition ($\Phi = 0.1$, $\tau = 0.25$ s for FR1). This was coupled to the sensitivity analysis to the H_2S mass fraction, carried out for the 3 datasets obtained for FR2 and FR1. To get a common reference, the conditions corresponding to the H_2 peak were considered, at the reactor coordinate where 1% H_2S conversion was achieved. Results are shown in Fig. 13. The combined analysis of flux and sensitivity analyses highlight a common behavior: the main reaction sustaining reactivity is the H-abstraction of the S radical on H_2S (R15). Although it might sound counterintuitive, since S radicals are more reactive than SH, this is explained by flux analysis (Fig. 13a), showing that R15 actually acts in the opposite direction: after SH is obtained via H-abstraction by H, O, OH, it provides back H_2S and releases an S radical. This last radical is quickly oxidized to SO and SO_2 via R16 and R17, releasing an O radical for each of these steps and further enhancing the reactivity process. In parallel to R15, R6 plays a crucial role in controlling the reactivity, since it is the primary source of SH radicals, then fed to R15b. On the other hand, the H_2S thermal decomposition (R1) does not play a significant role in such conditions, due to the high activation energy and the relatively low temperatures at stake to be of major significance.

4. Conclusions

The transition towards non-conventional energy sources has increased the scientific interest in H_2S treatment, such that a renewed attention towards its combustion chemistry has risen. On the other hand, the scarce amount of available data on its kinetic behavior at low temperatures, and under diluted conditions, have limited so far a complete understanding of both its pyrolysis and oxidation chemistry. In order to fill this lack of knowledge, this work presents experiments performed in three different (and complementary) ideal facilities, respectively a jet-stirred reactor and two flow reactors, with the aim to perform a multi-parametric study with a variable temperature, residence time and equivalence ratio. All the reactors were also coated with a boric oxide layer, thus limiting surface effects to a minimum. At the same time, the key reaction steps and branching ratios, identified *a priori* via literature analysis and sensitivity analysis, were theoretically investigated via an *ab initio* approach. Thus, the rates of the H-abstractions on H_2S by H and OH were calculated, as well as the channels of the reaction between SH and HO_2, providing either $H_2S + O_2$ (termination), or HSO + OH (propagation). These were included in a kinetic mechanism, also implementing the state-of-the-art kinetic rates on both H_2/O_2 and sulfur mechanisms.

Following a hierarchical approach, the combined use of the different reactors first allowed to explore the pyrolysis behavior of H_2S at low, intermediate, and high temperatures. The kinetic model was found to satisfactorily reproduce the conversion rates to H_2 and S_2 under all of the explored conditions, with the controlling step being only the fuel thermal decomposition to H_2 and S. In a second stage, H_2S oxidation was studied with the same methodology. The effect of oxygen addition was explored in the jet-stirred reactor at low-temperature, finding out a progressively earlier reactivity onset with increasing oxygen amount. In this context, the critical role of HO_2 could be highlighted as a reactivity enhancer, and with very high amounts of oxygen, the H-abstraction on H_2S by HO_2 itself plays a significant role in feeding the SH radical pool necessary to start the conversion process. At higher temperatures (i.e., in the two flow reactors), a key step was instead represented by the SH + SH reaction, i.e., reverse H-abstraction of S radical on the fuel. Indeed, this was found to act as a reactivity booster, providing the very reactive S radicals, on turn oxidized by O_2 to SO and then to SO_2, releasing O radicals in each of these steps.

Declaration of Competing Interest

The authors declare that they have no known competing financial interests or personal relationships that could have appeared to influence the work reported in this paper.

Acknowledgements

This work has been carried out under the financial support of the IMPROOF project (H2020-IND-CE-2016-17/H2020-SPIRE-S016) within the European Union Horizon 2020 research and innovation program (grant agreement no. 723706).

Appendix A. Supplementary data

Supplementary data to this article can be found online at https://doi.org/10.1016/j.cej.2022.136723.

References

[1] V. Paolini, F. Petracchini, M. Segreto, L. Tomassetti, N. Naja, A. Cecinato, J. Environ, Sci. Heal. Part A Toxic/Hazardous Subst, Environ. Eng. 53 (10) (2018) 899–906.
[2] S. Rasi, A. Veijanen, J. Rintala, Energy 32 (8) (2007) 1375–1380.
[3] Y. Han, Y. Zhang, C. Xu, C.S. Hsu, Fuel 221 (2018) 144–158.
[4] European Commission, Off. J. Eur. Union (L 338/87) (2009).
[5] T.L. Guidotti, Int. J. Toxicol. 29 (6) (2010) 569–581.
[6] C.H. Bartholomew, Appl. Catal. A Gen. 212 (1–2) (2001) 17–60.
[7] L. Appels, J. Baeyens, J. Degrève, R. Dewil, Prog. Energy Combust. Sci. 34 (6) (2008) 755–781.
[8] J. Zaman, A. Chakma, Fuel Process. Technol. 41 (2) (1995) 159–198.
[9] O. Mathieu, F. Deguillaume, E.L. Petersen, Combust. Flame 161 (1) (2014) 23–36.
[10] S. Gersen, M. Van Essen, H. Darmeveil, H. Hashemi, C.T. Rasmussen, J. M. Christensen, P. Glarborg, H. Levinsky, Energy and Fuels 31 (3) (2017) 2175–2182.
[11] J.M. Colom-Díaz, M. Leciñena, A. Peláez, M. Abián, Millera, R. Bilbao, M.U. Alzueta, Fuel 262 (2020).
[12] D.S. Chamberlin, D.R. Clarke, Ind. Eng. Chem. 20 (10) (1928) 1016–1018.
[13] L. Cohen, Fuel 34 (1955) S119–S122.
[14] G.J. Gibbs, H.F. Calcote, J. Chem. Eng. Data 4 (3) (1959) 226–237.
[15] Flockenhaus C, Gaswaerme Int. (1969).
[16] E.L. Merryman, A. Levy, J. Air Pollut. Control Assoc. (1967).
[17] E.L. Merryman, A. Levy, J. Phys. Chem. (1972).
[18] H.A. Olschewski, J. Troe, H.G. Wagner, J. Phys. Chem. 98 (49) (1994) 12964–12967.
[19] D. Woiki, P. Roth, J. Phys. Chem. 98 (49) (1994) 12958–12963.
[20] H. Shiina, M. Oya, K. Yamashita, A. Miyoshi, H. Matsui, J. Phys. Chem. 100 (6) (1996) 2136–2140.
[21] K. Tsuchiya, K. Yamashita, A. Miyoshi, H. Matsui, J. Phys. Chem. 100 (43) (1996) 17202–17206.
[22] K. Karan, A.K. Mehrotra, L.A. Behie, AIChE J. 45 (2) (1999) 383–389.
[23] K.A. Hawboldt, W.D. Monnery, W.Y. Svrcek, Chem. Eng. Sci. 55 (5) (2000) 957–966.
[24] M. Frenklach, J.H. Lee, J.N. White, W.C. Gardiner, Combust. Flame 41 (C) (1981) 1–16.
[25] O. Mathieu, C. Mulvihill, E.L. Petersen, Proc. Combust. Inst. 36 (3) (2017) 4019–4027.
[26] C. Zhou, K. Sendt, B.S. Haynes, Proc. Combust. Inst. 34 (1) (2013) 625–632.
[27] Y. Song, H. Hashemi, J.M. Christensen, C. Zou, B.S. Haynes, P. Marshall, P. Glarborg, Int. J. Chem. Kinet. 49 (1) (2017) 37–52.

[28] J.M. Colom-Díaz, M. Abián, M.Y. Ballester, A. Millera, R. Bilbao, M.U. Alzueta, Proc. Combust. Inst. 37 (1) (2019) 727–734.
[29] J.M. Colom-Díaz, M. Abián, Millera, R. Bilbao, M.U. Alzueta, Fuel 258 (2019).
[30] J. Peng, X. Hu, P. Marshall, J. Phys. Chem. A 103 (1999) 5307–5311.
[31] S.H. Mousavipour, M.A. Namdar-Ghanbari, L. Sadeghian, J. Phys. Chem. A 107 (19) (2003) 3752–3758.
[32] A. Montoya, K. Sendt, B.S. Haynes, J. Phys. Chem. A 109 (6) (2005) 1057–1062.
[33] K. Sendt, M. Jazbec, B.S. Haynes, Proc. Combust. Inst. 29 (2) (2002) 2439–2446.
[34] C. Zhou, Kinetic Study of the Oxidation of Hydrogen Sulfide -, The University of Sydney, 2009. PhD Thesis.
[35] C. Zhou, K. Sendt, B.S. Haynes, J. Phys. Chem. A 112 (14) (2008) 3239–3247.
[36] C. Zhou, K. Sendt, B.S. Haynes, J. Phys. Chem. A 113 (29) (2009) 8299–8306.
[37] C. Zhou, K. Sendt, B.S. Haynes, J. Phys. Chem. A 113 (12) (2009) 2975–2981.
[38] Y. Gao, C. Zhou, K. Sendt, B.S. Haynes, P. Marshall, Proc. Combust. Inst. 33 (1) (2011) 459–465.
[39] D. Bongartz, A.F. Ghoniem, Combust. Flame 162 (3) (2015) 544–553.
[40] T.Y. Cong, A. Raj, J. Chanaphet, S. Mohammed, S. Ibrahim, A. Al Shoaibi, Int. J. Hydrogen Energy 41 (16) (2016) 6662–6675.
[41] A. Raj, S. Ibrahim, A. Jagannath, Prog. Energy Combust. Sci. 80 (2020).
[42] A. Cavaliere, M. De Joannon, Prog. Energy Combust. Sci. 30 (4) (2004) 329–366.
[43] M. Zheng, M.C. Mulenga, G.T. Reader, M. Wang, D.S.K. Ting, J. Tjong, Fuel 87 (6) (2008) 714–722.
[44] S. Imtenan, M. Varman, H.H. Masjuki, M.A. Kalam, H. Sajjad, M.I. Arbab, I. M. Rizwanul Fattah, Energy Convers. Manag. 80 (2014) 329–356.
[45] A. Stagni, Y. Song, L.A. Vandewalle, K.M. Van Geem, G.B. Marin, O. Herbinet, F. Battin-Leclerc, T. Faravelli, Chem. Eng. J. 385 (2019), 123401.
[46] A. Stagni, C. Cavallotti, S. Arunthanayothin, Y. Song, O. Herbinet, F. Battin-Leclerc, T. Faravelli, React, Chem. Eng. 5 (4) (2020) 696–711.
[47] S. Arunthanayothin, A. Stagni, Y. Song, O. Herbinet, T. Faravelli, F. Battin-Leclerc, Proc, Combust, Inst, 2020.
[48] F. Battin-Leclerc, J.M. Simmie, E. Blurock, Cleaner Combustion - Developing Detailed Chemical Kinetic Models, Springer, 2013.
[49] A.C. Egerton, D.R. Warren, Proc, R. Soc. London. Ser. A. Math. Phys, Sci, 1951.
[50] R.R. Baldwin, L. Mayor, Trans. Faraday Soc. 56 (1960) 103–114.
[51] R.R. Baldwin, R.W. Walker, D.H. Langford, Trans. Faraday Soc. 65 (1969) 792–805.
[52] Z.H. Lodhi, R.W. Walker, J. Chem. Soc. Faraday Trans. 87 (5) (1991) 681–689.
[53] C. Cavallotti, M. Pelucchi, Y. Georgievskii, S.J. Klippenstein, J. Chem. Theory Comput. 15 (2) (2019) 1122–1145.
[54] M. Frisch, G. Trucks, H.B. Schlegel, G.E. Scuseria, M.A. Robb, J.R. Cheeseman, G. Scalmani, V. Barone, (2009).
[55] H.-J. Werner, P.J. Knowles, F.R. Manby, J.A. Black, K. Doll, A. Heßelmann, D. Kats, A. Köhn, T. Korona, D.A. Kreplin, Q. Ma, T.F. Miller, A. Mitrushchenkov, K. A. Peterson, I. Polyak, G. Rauhut, M. Sibaev, J. Chem. Phys 152 (2020), 144107.
[56] S.J. Klippenstein, J.A. Miller, J. Phys. Chem. A 106 (2002) 9267–9277.
[57] S. Grimme, S. Ehrlich, L. Goerigk, J. Comput. Chem. 32 (7) (2011) 1456–1465.
[58] J.M.L. Martin, Chem. Phys. Lett. 259 (5–6) (1996) 669–678.
[59] P.J. Knowles, H.J. Werner, Chem. Phys. Lett. 145 (6) (1988) 514–522.
[60] H. Werner, P.J. Knowles, J. Chem. Phys. 89 (9) (1998) 5803.
[61] J.A. Miller, S.J. Klippenstein, J Phys Chem A 110 (2006) 10528–10544.
[62] C. Eckart, Phys. Rev. 35 (11) (1930) 1303–1309.
[63] Y. Georgievskii, S.J. Klippenstein, J. Phys. Chem. A 107 (2003) 9776–9781.
[64] S.J. Klippenstein, J. Chem. Phys. 96 (1) (1998) 367.
[65] E.E. Greenwald, S.W. North, Y. Georgievskii, S.J. Klippenstein, J. Phys. Chem. A 109 (27) (2005) 6031–6044.
[66] J.A. Yuri Georgievskii, S.J. Miller, Klippenstein,, Phys. Chem. Chem. Phys. 9 (31) (2007) 4259–4268.
[67] L.B. Harding, Y. Georgievskii, S.J. Klippenstein, J. Phys. Chem. A 109 (2005) 4646–4656.
[68] E. Ranzi, A. Frassoldati, R. Grana, A. Cuoci, T. Faravelli, A.P. Kelley, C.K. Law, Prog. Energy Combust. Sci. 38 (4) (2012) 468–501.
[69] C. Wang, G. Zhang, Z. Wang, Q.S. Li, Y. Zhang, J. Mol. Struct. THEOCHEM 731 (1–3) (2005) 187–192.
[70] C.-W. Lu, Y.-J. Wu, Y.-P. Lee, R.S. Zhu, M.-C. Lin, J. Phys. Chem. A 107 (50) (2003) 11020–11029.
[71] N.L. Garland, Chem. Phys. Lett. 290 (4–6) (1998) 385–390.
[72] K. Sendt, B.S. Haynes, Proc. Combust. Inst. 31 (1) (2007) 257–265.
[73] A. Goumri, J.-D.-R. Rocha, D. Laakso, C.E. Smith, P. Marshall, J. Phys. Chem. A 103 (51) (1999) 11328–11335.
[74] H.J. Plach, J. Troe, Int. J. Chem. Kinet. 16 (12) (1984) 1531–1542.
[75] W.K. Metcalfe, S.M. Burke, S.S. Ahmed, H.J. Curran, Int. J. Chem. Kinet. 45 (10) (2013) 638–675.
[76] H. Shiina, A. Miyoshi, H. Matsui, J. Phys. Chem. A 102 (20) (1998) 3556–3559.
[77] M. Yoshimura, M. Koshi, H. Matsui, K. Kamiya, H. Umeyama, Chem. Phys. Lett. 189 (3) (1992) 199–204.
[78] Y. Kurosaki, T. Takayanagi, J. Chem. Phys. 111 (23) (1999) 10529.
[79] J. Qi, D. Lu, H. Song, J. Li, M. Yang, J. Chem. Phys. 146 (12) (2017), 124303.
[80] M.J. Kurylo, N.C. Peterson, W. Braun, J. Chem. Phys. 54 (3) (1971) 943.
[81] D. Mihelcic, R.N. Schindler, Berichte Der Bunsengesellschaft Für Phys, Chemie 74 (12) (1970) 1280–1288.
[82] Graham Pratt, David Rogers, J. Chem. Soc. Faraday Trans. 1 Phys. Chem. Condens. Phases 73 (1977) 54–61.
[83] P. Roth, R. Löhr, U. Barner, Combust. Flame 45 (C) (1982) 273–285.
[84] D. Lu, J. Li, J. Chem. Phys. 145 (1) (2016), 014303.
[85] A.A. Westenberg, N. deHaas, J. Chem. Phys. 59 (12) (1973) 6685.
[86] B.A. Ellingson, D.G. Truhlar, J. Am. Chem. Soc. 129 (42) (2007) 12765–12771.
[87] B. Du, W. Zhang, Comput. Theor. Chem. 1069 (2015) 77–85.
[88] L. Ping, Y. Zhu, A. Li, H. Song, Y. Li, M. Yang, Phys. Chem. Chem. Phys. 20 (41) (2018) 26315–26324.
[89] J.V. Michael, D.F. Nava, W.D. Brobst, R.P. Borkowskl, L.J. Stief, J. Phys. Chem 86 (1982) 81–84.
[90] Y.-L. Lin, N.-S. Wang, Y.-P. Lee, Int. J. Chem. Kinet. 17 (11) (1985) 1201–1214.
[91] I. Barnes, V. Bastian, K.H. Becker, E.H. Fink, W. Nelsen, J. Atmos. Chem. 1986 44 4 (4) (1986) 445–466.
[92] C. Lafage, J.-F. Pauwels, M. Carlier, P. Devolder, J. Chem. Soc. Faraday Trans. 2 Mol. Chem. Phys. 83 (5) (1987) 731–739.
[93] G.S. Tyndall, A.R. Ravishankara, Int. J. Chem. Kinet. 23 (6) (1991) 483–527.
[94] R.A. Perry, R. Atkinson, J.N.P. Jr, J. Chem. Phys. 64 (8) (1976) 3237.
[95] R.A. Cox, D. Sheppard, Nature 284 (5754) (1980) 330–331.
[96] M.-T. Leu, R.H. Smith, J. Phys. Chem 86 (1) (1982) 73–81.
[97] C.L. Lin, Int. J. Chem. Kinet. 14 (5) (1982) 593–598.
[98] Q. De Wang, M.M. Sun, J.H. Liang, Comput, Theor. Chem. 1155 (2019) 61–66.
[99] A.M. Starik, V.A. Savelieva, A.S. Sharipov, N.S. Titova, Combust. Flame (2016).